

Ocean Surface Turbulence in Newly Formed Marginal Ice Zones

Madison Smith  and Jim Thomson 

Applied Physics Laboratory, University of Washington, Seattle, WA, USA

Key Points:

- Near-surface turbulence in new marginal ice zones can be estimated using wind stress and a parameterized effective transfer velocity
- When waves are large (despite attenuation in ice), effective transfer velocity is reduced at a rate related to ice volume and wave height
- When waves are small and ice cover is high, effective transfer velocity is related to the velocity of the ice relative to the ocean below

Supporting Information:

- Supporting Information S1

Correspondence to:

M. Smith,
mmsmith@apl.washington.edu

Citation:

Smith, M., & Thomson, J. (2019). Ocean surface turbulence in newly formed marginal ice zones. *Journal of Geophysical Research: Oceans*, 124, 1382–1398. <https://doi.org/10.1029/2018JC014405>

Received 24 JUL 2018

Accepted 26 JAN 2019

Accepted article online 1 FEB 2019

Published online 1 MAR 2019

Abstract Near-surface turbulent kinetic energy dissipation rates are altered by the presence of sea ice in the marginal ice zone, with significant implications for exchanges at the air-ice-ocean interface. Observations spanning a range of conditions are used to parameterize dissipation rates in marginal ice zones with relatively thin, newly formed ice, and two regimes are identified. In both regimes, the turbulent dissipation rates are matched to the turbulent input rate, which is formulated as the surface stress acting on roughness elements moving at an effective transfer velocity. In marginal ice zones with waves, the short waves are the roughness elements, and the phase speed of these waves is the effective transfer velocity. The wave amplitudes are attenuated by the ice, and thus, the size of the roughness elements is reduced; this is parameterized as a reduction in the effective transfer velocity. When waves are sufficiently small, the ice floes are the roughness elements, and the relative velocity between the sea ice and the ocean is the effective transfer velocity. A scaling is introduced to determine the appropriate transfer velocity in a marginal ice zone based on wave height, ice thickness and concentration, and ice-ocean shear. The results suggest that turbulence underneath new sea ice is mostly related to the wind forcing and that marginal ice zones generally have less turbulence than the open ocean under similar wind forcing.

Plain Language Summary The rate of mixing near the ocean's surface determines the rate of exchange of material, heat, and energy between the air and the ocean. Determining the rate of mixing under all conditions is necessary to be able to make global estimates of exchange, such as how much carbon dioxide is going into the ocean. In the open ocean, this rate can be predicted using measurements of the wind. In oceans where sea ice is present, the rate is lower. The current methods for predicting the rate of surface mixing in sea ice are too simple and do not well describe the range of conditions that occur. We propose that this rate can be predicted in thin, new sea ice using measurements of waves, wind, and the ice. When ocean waves are present, the rate of mixing is predicted to increase with increasing wave height and decrease with increasing ice. When there are no waves, we can predict the approximate rate of mixing due to wind stress using the speed of the ice relative to the ocean. Under all conditions, the rate of mixing in sea ice-covered oceans is expected to be lower than in open ocean with the same wind.

1. Introduction

The turbulent kinetic energy (TKE) dissipation rate at the air-sea interface in ice-covered regions controls exchanges of heat, momentum, and gas transfer. The amount of wind-driven TKE in the ocean's near-surface region changes as a function of waves, as well as the sea ice cover. Near-surface turbulence remains the least constrained in ice-covered regions, which can cover up to 10% of the world's oceans. This is particularly important for improving parametric models for air-sea gas exchange in the marginal ice zone (MIZ), which utilize estimates of TKE dissipation rates (Loose et al., 2014). The impact of sea ice on air-sea gas exchange may vary widely, as the presence of sea ice can both enhance exchange by causing stirring and inhibit exchange by serving as a barrier (Bigdeli et al., 2018).

In the MIZ, the flux of momentum from the wind (i.e., the wind stress τ_{wind}) is transmitted to the ocean below via drag on both open water patches and ice floes. It is common to partition the wind stress as

$$\tau_{\text{wind}} = (1 - A)\tau_{\text{air-water}} + A\tau_{\text{ice-water}}, \quad (1)$$

where A is fractional areal coverage of sea ice (e.g., Steele et al., 1989; Yang, 2006). The first term represents the stress from the wind on open water patches, and the second term represents the stress from the wind on

ice floes. Although a useful framework for many studies, this partitioning of the wind forcing may not be an accurate representation of a MIZ in which the ice floes, and open water patches are acting as a continuum on scales much smaller than the turbulent eddies in the atmosphere. Further, this partitioning is unnecessary to determine the total momentum flux to the ocean below (τ_{ocean}) if there is no significant acceleration of floes, such that the momentum flux must be conserved as $\tau_{\text{wind}} = \tau_{\text{ocean}}$. In the simplified case of constant wind forcing, a steady-state momentum balance from the wind to the water can be established through a constant relative ice-ocean velocity (Δu).

Here we investigate ocean turbulence just below the MIZ as a function of the total wind stress τ_{wind} , with the implicit assumption that $\tau_{\text{wind}} = \tau_{\text{ocean}}$. Wind stress is estimated for observations using the covariance methods, which inherently integrates spatial conditions. This approach avoids partitioning momentum between open and ice-covered areas and also avoids specification of ice-ocean drag coefficient, because total momentum flux is simply conserved through the air-water-ice interface of the MIZ.

The rate at which the wind stress τ_{wind} does work on the ocean can be related to the effective speed c_e at which the dynamic roughness elements (creating surface drag) move with that stress. The rate of wind work, $c_e \tau_{\text{wind}}$, has been used in previous studies to define the input flux of TKE to the ocean by the wind. The dynamic roughness elements at the surface in open water are short waves, and the effective transfer velocity for wind work is thus related to the phase speed of the waves (Gemmrich et al., 1994). Several studies in ice-free regions have shown that this input rate of TKE is in balance with the TKE dissipation rate ϵ integrated over an active layer depth as (Terray et al., 1996; Thomson et al., 2016):

$$c_e \tau_{\text{wind}} \approx \rho \int \epsilon(z) dz. \quad (2)$$

Thus, in ice-free regions, the turbulent dissipation rate ϵ is often parameterized using the wind stress and an effective transfer velocity related to wave phase speed. As the roughness of the open ocean is primarily dependent on the short waves, it has been found that a typical open water effective transfer velocity is approximately $c_{e0} \approx 2$ m/s (Thomson et al., 2016). This value can be adjusted according to the wave age, which is the ratio of the phase speed at the peak of the wave spectrum to the wind speed, c_p/U_{10} (Terray et al., 1996). It should be noted that these formulations for TKE in ice-free areas are much larger than law-of-the-wall estimates would suggest, because breaking surface waves directly inject turbulence at much higher rates than shear production can supply (Agrawal et al., 1992). This approach then inherently neglects viscous stresses, which are likely to be much smaller than wave-supported stresses in all but the lowest wind conditions (e.g., Grare et al., 2018).

One previous study has applied this model for wind work via an effective transfer speed to a MIZ. Zippel and Thomson (2016) found the effective transfer speed to be a function of ice concentration, in addition to wave speed. Waves decrease in amplitude with distance into the MIZ due to attenuation processes. The Zippel and Thomson (2016) study showed that the attenuation of waves with increasing ice concentration in the MIZ reduced the growth rate of waves due to the wind. Thus, ice reduced the amplitude of the roughness elements and thereby the wind work and associated TKE input rate. This prior study used observations in an old MIZ with melting ice floes. Here we apply observations in several newly forming (freezing) MIZs and test the dependence of the effective transfer velocity on wave and ice conditions. It is expected that the effective transfer speed in such MIZs may have a dependence on both ice concentration and thickness, as the amplitude of the short waves, which typically dominate the roughness at the ocean surface, is strongly related to the volume of ice.

When there is sufficient ice such that waves are small or absent, the roughness of the surface is dominated by the ice, rather than the waves. The roughness elements then move at a speed relative to the ocean that is set by the velocity of the sea ice. The present study tests this relative ice-ocean velocity as an effective transfer velocity of wind work to determine the input rate of TKE to the upper ocean. We retain the framework of equation (2), where the input rate of TKE from wind through ice balances the TKE dissipation. We identify this as a distinct regime, in which the input rate c_e is determined by the motion of the ice rather than by the motion of the waves.

In addition to the mechanical forcing of wind work, buoyancy flux (B) may be important in ice-covered oceans due to the generation of dense, salty water with ice formation (e.g., the brine rejection reviewed in Morison et al., 1992). Recent observational work in the Canada Basin by Gallaher et al. (2016) evaluated

thermodynamic evolution of the upper ocean and local freshwater and associated buoyancy fluxes. They found buoyancy fluxes equivalent to a TKE flux on the order of 10^{-8} to 10^{-7} m^2/s^3 . In comparison, previous estimates of near-surface turbulence in the Canada Basin MIZ were on the order of 10^{-5} to 10^{-3} m^2/s^3 (Zippel & Thomson, 2016). The buoyancy term in this region is relatively small, and the mechanical input at the air-ice or ice-ocean interface likely is the dominant source of TKE.

Another potential source of TKE input to the ocean surface layer, in addition to wind work, is the turbulence generated directly by wave-ice interactions. It is well-established that dissipative processes cause nonconservative attenuation of wave energy in the MIZ, but the exact mechanisms remain unknown. Possible mechanisms include drag at the base of the ice layer, viscous drag within the ice layer, breakup of floes, and inelastic floe-floe collisions. In the absence of wind (i.e., swell conditions), waves might cause ice floes to move relative to the water below and dissipate wave energy in the form of turbulence. This process has been suggested to be especially dominant in thin, new ice types (Kohout & Meylan, 2008) and for long period waves (Ardhuin et al., 2016). Doble and Bidlot (2013) found that inclusion of this parameterization in a wave model improved agreement with observations of waves in sea ice. Although turbulence production by ice-ocean drag has been proposed as an important mechanism for attenuation of wave energy in sea ice, there have been no direct observations of this relationship to our knowledge. This mechanism is difficult to isolate in the present study, because most of the conditions have young waves that are strongly correlated with the local winds (i.e., no swell conditions are observed). In the chosen framework for this study, the local winds provide all of the forcing, and waves mediate that forcing without directly providing additional input. Although this approach may be incomplete, in terms of mechanisms, it has an advantage of being completely local (i.e., it does not require knowledge of spatial gradients in wave energy flux through the MIZ).

In the following sections, we use observations of turbulent dissipation rates in open water and new pancake and frazil ice cover to explore how turbulence is altered in the MIZ. Central to this approach is an assumption that wind work generates turbulence at a rate given by the wind stress and an effective transfer speed and that turbulence is then dissipated locally in the ocean surface layer. To match the observations, we define parameterizations for effective transfer velocities based on wave and ice conditions. We present three regimes, each with an example case.

1. In the ice-free open ocean, the effective transfer velocity is related to wave phase speed.
2. In thin ice when the sea state is relatively high, the effective transfer velocity is reduced relative to open water as a result of damping by ice.
3. In thin ice when the sea state is low, either due to low wind or strong wave attenuation, the effective transfer velocity is related to the relative velocity between ice and ocean.

After presenting these results, we discuss the transition point between these regimes and limitations of the framework. Finally, we briefly evaluate the implications for near-surface turbulence as a possible mechanism for wave attenuation (i.e., direct wave energy loss) in the MIZ.

2. Methods

This study uses upper-ocean turbulent dissipation rate profiles from field campaigns in both the Arctic and Antarctic MIZ during autumn ice advance. Vertical profiles of dissipation rates, $\epsilon(z)$, in the upper 0.5 m of the ocean were made using a Nortek 2 MHz Aquadop HR Doppler profiler installed on Surface Wave Instrument Floats with Tracking (SWIFTs; Thomson, 2012). We will first describe the field campaigns and data collection and then describe the instrument and turbulent dissipation rate data processing methods.

2.1. Field Campaigns

Around 350 hr of SWIFT buoy data were obtained in the Beaufort and Chukchi Seas in the Arctic Ocean during the *Arctic Sea State* field campaign, which took place from 01 October to 10 November 2015 on the *R/V Sikuliaq*. An overview of the field campaign can be found in Thomson et al. (2018), with further details in the referenced papers. Additionally, we will use approximately 5 hr of measurements obtained in the Ross Sea in the Antarctic during the *Polynyas and Ice Production in the Ross Sea* field campaign from 11 April to 14 June 2017 on the *R/V Palmer*. Locations of buoy deployments made during these two field campaigns that will be utilized in this study are shown in Figure 1.

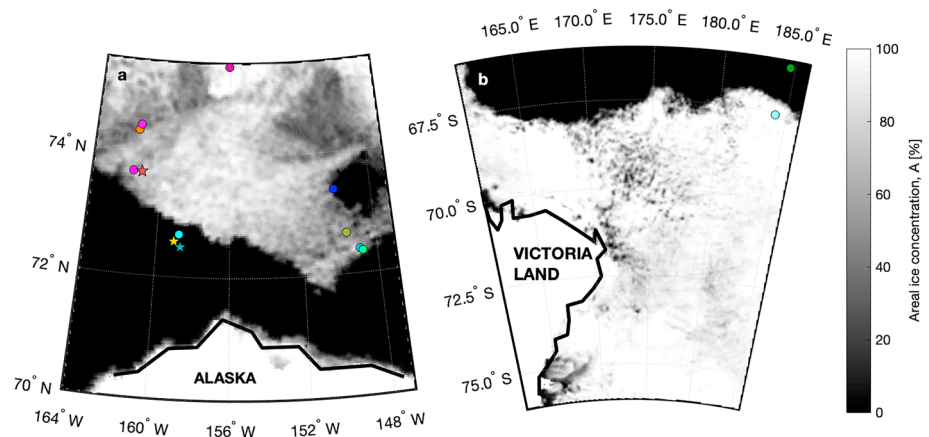


Figure 1. Map of SWIFT deployments in (a) Beaufort Sea, Arctic Ocean (2015), and (b) Ross Sea, Southern Ocean (2017). Gray scale shading indicates ice concentration from AMSR2 (Spren et al., 2008) where white indicates 100% ice cover and black represents open water. Each colored point represents one SWIFT deployment, where the color corresponds with deployments used in subsequent plots, and stars indicate those shown in example plots in section 3.1. Conditions observed during each deployment are summarized in Table 1.

Deployments span three different regimes describing how momentum from wind stress is transferred to near-surface turbulence: open water, “wave-transferred” MIZ, and “ice-transferred” MIZ. Images of example conditions during each of these regimes are shown in Figure 2, and complete time series and profile data corresponding to each of these examples follow in section 3.1. Open water deployments were separated based on images taken by the buoys and recorded ship-based observations. Wave-transferred and ice-transferred MIZ deployments were categorized primarily based on ice concentration, with the ice-transferred regime expected to occur when ice concentrations were over 80% and waves were small. Deployments that did not clearly fall into one regime or had multiple regimes represented over time were not used. Conditions during all deployments used in subsequent analysis are summarized in Table 1. Time series and profiles for all deployments are given in Supporting Information S1.

Ship-based measurements of key parameters are collocated with buoy measurements when they are within 5 km. During both field campaigns, visual observations of sea ice were made hourly following the Antarctic Sea ice Processes and Climate protocol, which includes estimates of ice thickness (z_{ice}) and areal concentration (A). This protocol was developed by the Antarctic Sea ice Processes and Climate group in 1997 as a standard method for sea ice observations made by ships in the Antarctic pack ice and has since been applied widely over the Arctic and Antarctic (Worby, 1999). Visual estimates of ice thickness are reasonable, with an error of approximately 30% for thicknesses less than 30 cm (Worby et al., 2008). Additional estimates of ice thickness were made during the Arctic Sea State campaign using a thermodynamic technique based on surface temperatures measured by rail-mounted Heitronics KT-15 infrared 421 thermometers (Persson et al.,

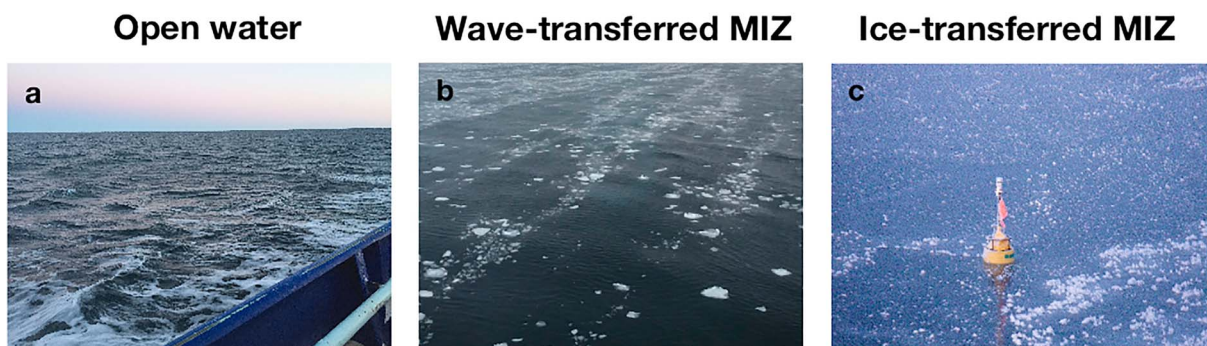


Figure 2. Photos taken from the *R/V Sikuliaq* of examples of the three turbulence generation regimes explored: (a) open water; (b) marginal ice zone (MIZ) with wind-work transferred via waves; and (c) MIZ with wind-work transferred via ice.

Table 1

Summary of Conditions for All SWIFT Deployments in Open Water, Wave-Transferred Marginal Ice Zones, and Ice-Transferred Marginal Ice Zones Used in This Study

Date	U_{10} (m/s)	H_s (m)	Δu (m/s)	z_{ice} (m)	A (%)	C_d
Open water						
02 Oct 2015	10.5–11.7	0.95–1.2	N/A	N/A	0	1.2×10^{-3}
04 Oct 2015	6.7–11	0.4–0.6	N/A	N/A	0	1.2×10^{-3}
23–24 Oct 2015 (a)*	7.2–15	0.93–1.5	0.08–0.41	N/A	0	1.4×10^{-3}
Wave-transferred marginal ice zone						
10 Oct 2015	4.8–11	0.17–0.54	0.22–0.75	0.03–0.04	32–46	$1.4 \times 10^{-3}^{\wedge}$
11–14 Oct 2015 (a)	8.9–26	2.0–4.3	0.03–0.40	0.02–0.05	15–24	1.2×10^{-3}
23–24 Oct 2015 (b)	16–29	0.12–1.4	N/A	0.02–0.09	13–50	1.4×10^{-3}
03 June 2017	8.7–12	0.35–0.80	N/A	0.2–0.3	100	$1.4 \times 10^{-3}^{\wedge}$
05 June 2017	4.6–14	2.3–3.9	N/A	0.5	70–80	$1.4 \times 10^{-3}^{\wedge}$
11–14 Oct 2015 (b)	4.0–27	2.4–4.5	0.01–0.40	0.02–0.04	6–30	1.5×10^{-3}
11–13 Oct 2015	10–19	1.2–3.9	0.01–0.40	0.06–0.1	40–85	1.4×10^{-3}
25–27 Oct 2015*	3.2–10	0.02–0.37	0.02–0.32	0.14	6–80	1.3×10^{-3}
Ice-transferred marginal ice zone						
16–18 Oct 2015 (a)	4.0–9.0	0.06–0.30	0.02–0.56	0.08–0.1	82–85	0.8×10^{-3}
06–08 Oct 2015	2.3–7.8	0.01–0.02	0.01–0.36	0.15	99–100	0.6×10^{-3}
16–18 Oct 2015 (b)*	0.3–5.4	0.01–0.34	0.02–0.56	0.08–0.5	83–93	0.7×10^{-3}

Note. Deployments with * after the date correspond to examples shown in Figures 3–8. Deployments in 2015 all occurred in the Beaufort Sea, and deployments in 2017 occurred in the Ross Sea. Range of values for wind speed and wave heights are from SWIFT buoy measurements, near-surface change in velocity values is determined from a collocated SWIFT with downward-looking Aquadopp, and ice thickness and areal concentration are from ship-based visual estimates. Average air-ocean drag coefficients (C_d) shown are based on observed values collocated from the ship, except where noted by \wedge , indicating constant value of 1.4×10^{-3} is used.

2018; Wadhams et al., 2018). This method builds on satellite-based algorithms by Yu and Rothrock (1996) and Wang et al. (2010) to use measurements of skin temperature, wind, ocean freezing temperature, and energy fluxes to estimate ice thickness over approximately 3-m spots with the surface energy budget. Estimates from visual observations and the thermodynamic method will be referred to as simply visual and thermodynamic subsequently. As we were primarily making measurements in newly formed sea ice, thickness and concentration typically varied over the scale of a few kilometers. This is typically a large enough area to represent the scale for which direct wind stress measurements integrate over.

Wind stress is calculated using observed wind speed from buoys and best estimates of drag coefficients from the ship. As the surface drag coefficient C_d can vary by nearly an order of magnitude with different types of ice cover (Guest & Davidson, 1991), collocated 10-min average measurements made from the ship using the covariance method during the Arctic Sea State field campaign are used when available (Persson et al., 2018). These measurements are significantly lower than previous bulk estimates of drag coefficients in the MIZ; estimates in pancake ice during this field experiment were typically around 1.2×10^{-3} , whereas estimates using the scheme from SHEBA (Persson et al., 2002) were around 1.8×10^{-3} . As collocated drag coefficients are available only sporadically, an average drag coefficient is determined for each buoy deployment. Deployments typically span a day or two or as little as a few hours. When ship-based measurements are unavailable (as is the case for all Ross Sea deployments), the air-ocean drag coefficient is assumed as the median of the observed values: $C_d = 1.4 \times 10^{-3}$. The use of a single drag coefficient for each deployment is justified by low range in the collocated coefficients, typically less than 20% of the average value, such that variation in wind stress is mostly captured by the variation in the wind speed. Air-side friction velocity is determined using wind velocity (measured by SWIFT buoys) as $u_{*a} = \sqrt{C_d U_{10}^2}$. Then, the ocean friction velocity u_* is calculated from air-side friction velocity using the ratio of air density (ρ_a) to average water density (ρ_w), as

$$u_* = u_{*a} \sqrt{\rho_a / \rho_w} \quad (3)$$

We assume constant air and water densities of 1.225 and 1,025 kg/m³, respectively. Total wind stress imparted on the ocean is then calculated using the ocean friction velocity as

$$\tau_{\text{wind}} = \rho_w u_*^2. \quad (4)$$

Following the assumption that ice is not accelerating, this is assumed to be equal to the total stress τ_{ocean} received by the ocean beneath the MIZ (i.e., $\tau_{\text{ocean}} = \tau_{\text{wind}}$).

2.2. SWIFT Buoys

Surface ocean and atmospheric measurements during both field campaigns were made using SWIFT buoys. SWIFT are a freely drifting, surface following platform designed primarily to measure waves and near-surface turbulence. The relevant systems will be briefly described here, but further details of the platform and systems can be found in Thomson (2012) and Smith et al. (2018).

The top of the 1-m mast is equipped with an Airmar PB200 ultrasonic anemometer measuring wind speed and direction and a uCAM serial camera which takes images of the surface every 4 s (although image quality is limited by daylight and formation of ice over the camera lens). A Microstrain 3DM-GX3-35 combination GPS receiver and Inertial Motion Unit at the ocean surface height in the hull of the buoy is used to obtain wave spectra and bulk parameters. An AADI Aanderaa Conductivity Sensor mounted on the hull of the SWIFT (0.5-m below the surface) is used to measure temperature and salinity at 1 Hz, with a response time of ~ 10 and ~ 3 s, respectively. Although bulk changes in density ρ_w over time can be observed, the response time of the instrument is not sufficient to calculate buoyancy flux.

SWIFTs used throughout this study were deployed with a Nortek Aquadopp HR mounted upward-looking on the hull of the buoy. Velocity measurements from the upward-looking Aquadopp HR are used to calculate turbulent dissipation, as described in the next section. Some SWIFT drifters equipped with a Nortek Aquadopp mounted downward-looking on the hull were deployed in tandem with SWIFTs with upward-looking Aquadopp HRs. Downward-looking Aquadopp measure velocity profiles from 1.5 to 21 m below the surface in 0.5-m bins. SWIFT buoys have been shown to drift with ice at the surface within 1% (Lund et al., 2018) such that the observed velocity can be assumed to represent the change in velocity between the ice and ocean. Then, Δu is estimated as relative velocity between the ice and ocean 1.5 m below the surface, which is measured by the first bin of the Aquadopp profiler. Values of δu from simultaneously deployed downlooking SWIFTs (when available) are collocated with uplooking SWIFTs, which are as far as 10 km apart.

2.3. TKE Dissipation

Nortek Aquadopp HRs were mounted facing upward from 0.8-m below the surface on the hull of SWIFT drifters (Thomson, 2012). Beam 1, which is used for turbulent dissipation rate calculations, is oriented approximately 60° counterclockwise from the wind vane, to avoid measuring the wake of the buoy. Profiles are truncated at 0.5-m subsurface to remove known hull interference at the bottom of profiles.

Along-beam velocity profiles $u(z)$ are recorded by the Aquadopp at 4 Hz in 4-cm bins. Basic quality control is completed to remove velocity measurements with return amplitude and pulse correlation less than 30 and 50, respectively. These cutoffs were empirically determined by Thomson (2012) as the maximum corresponding to profiles out of the water and spurious points. Quality-controlled velocity records are used to calculate average and turbulent (root-mean-square) velocity profiles.

Dissipation is then estimated from velocity profiles using the second-order structure function, which is robust to SWIFT platform motion. The structure function is defined as

$$SF(z) = \langle [u(z) - u(z+r)]^2 \rangle, \quad (5)$$

where z is the bin depth, and r is the distance between bins (Wiles et al., 2006). Turbulent dissipation profiles $\epsilon(z)$ are estimated by fitting the structure function to a $r^{2/3}$ dependence following the methods in Thomson (2012) and Zippel and Thomson (2016). This method has been validated by comparison with ADV point measurements of dissipation (Thomson, 2012) and dissipation profiles estimated using frequency spectra (Zippel et al., 2018). The application of the structure function here varies from previous applications primarily in that it uses only measurements within six bins of each depth ($6r$) and is double-sided.

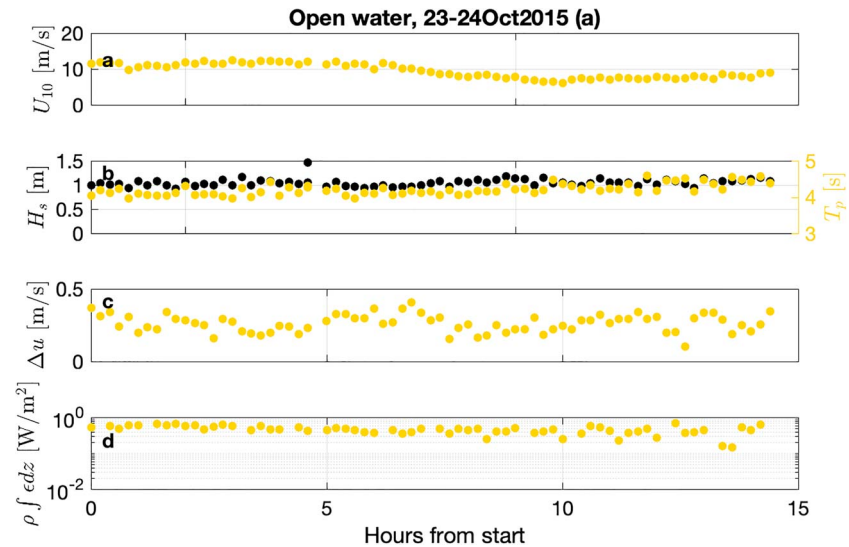


Figure 3. Time series from a SWIFT deployed in open water, 23 – 24 October 2015 (a) of (a) wind speed, (b) significant wave height and peak wave period, (c) relative velocity of ice and ocean (at 1.5-m depth), and (d) vertically integrated turbulent kinetic energy dissipation rates.

When sea ice is present, reflections from ice at the surface and suspended ice particles in the water column can result in erroneous Aquadopp velocity measurements. Two quality control steps are applied to data to account for this. First, we remove data at and above bins with spikes in correlation and amplitude that result from reflections. This approach is similar to methods that have been long used to measure ice draft with uplooking Sonar and more recently extended to uplooking Acoustic Doppler Current Profilers (ADCPs; Lohrmann et al., 2011; Magnell et al., 2010). When correlation exceeds 98% or amplitude exceeds 195, it is presumed that ice is present, and velocity measurements will not provide accurate estimates of turbulence. The removal of data via this process is referred to as an “ice mask.” In some cases, erroneously high velocity measurements as a result of ice contamination do not correspond to high amplitude or correlations and result in additional peaks in the distribution of raw velocity data. Bursts of data where there is more than one significant peak in the velocity distribution are completely removed, and dissipation rates are not calculated. Of all data in the wave-transferred MIZ, approximately 3.3% of bursts are removed due to multiple peaks in the velocity distribution, and approximately 39% of the remaining data are removed as a result of other quality control metrics. Of all data in the ice-transferred MIZ, approximately 14% of bursts are removed due to multiple peaks in the velocity distribution, and approximately 34% of the remaining data are removed as a result of other quality control metrics.

3. Results

3.1. Examples

3.1.1. Open Water (No Ice) Example

Time series of the wind speed, significant wave height, peak wave period, relative ice-ocean velocity, and integrated near-surface turbulent dissipation rates are shown for an open water example, 23 – 24 October 2015 (a), in Figure 3. Peak wave period, T_p , is related to the wave age (c_p/U_{10}) by the wave phase speed, calculated using the deep-water dispersion relation, $c_p = \frac{gT_p}{2\pi}$. Figure 4 shows Aquadopp HR data following quality control and processing for the same example. In open water, it is typical to see moderately high amplitudes and correlations throughout the water column. Turbulent velocities and dissipation generally peak at the surface as a result of input from breaking waves, and these parameters decay with depth (e.g., Thomson et al., 2016).

3.1.2. Wave-Transferred MIZ Example

The time series in Figure 5 shows an example of conditions encountered during a deployment in a wave-transferred MIZ. In addition to variables shown in Figure 3, Figure 5c shows the ice thickness and concentration, which are increasing over time in this example. Figure 6 shows the Aquadopp HR data following quality control and processing specific to observations in sea ice cover. Initially, dissipation profiles

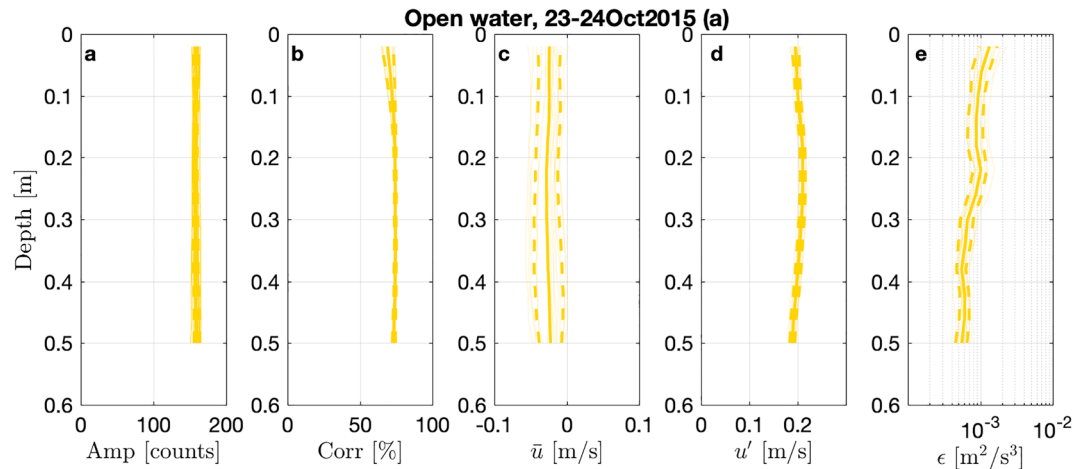


Figure 4. Aquadopp burst data from SWIFT deployed in open water, 23 – 24 October 2015 (a). Vertical profiles of (a) amplitude, (b) pulse correlation, (c) average velocity, (d) turbulent velocity, and (e) dissipation rate.

are similar in shape and magnitude to those observed in open water. The correlation and amplitude values are moderate, such that dissipation rate can be calculated over the entire profile. As sea ice thickness and concentration increase over time, turbulent velocities and dissipation rates rapidly decrease. The ice mask is applied to the later profiles at and above depths with high correlations or amplitudes, which is indicated by the gray shading in Figure 6. The depth of the ice mask provides an estimate of sea ice thickness (Figure 5c), in addition to the thickness estimates from the shipboard sampling.

3.1.3. Ice-Transferred MIZ Example

The example of Aquadopp HR data following quality control and processing in a ice-transferred MIZ in Figure 8, with corresponding time series in Figure 7, shows a more extreme application of this quality control. (Note that the change in upper ocean velocity, Δu , is from a collocated buoy deployed later, and no values are available for the first 11 hr.) Here the upper bins of the dissipation profile cannot be calculated

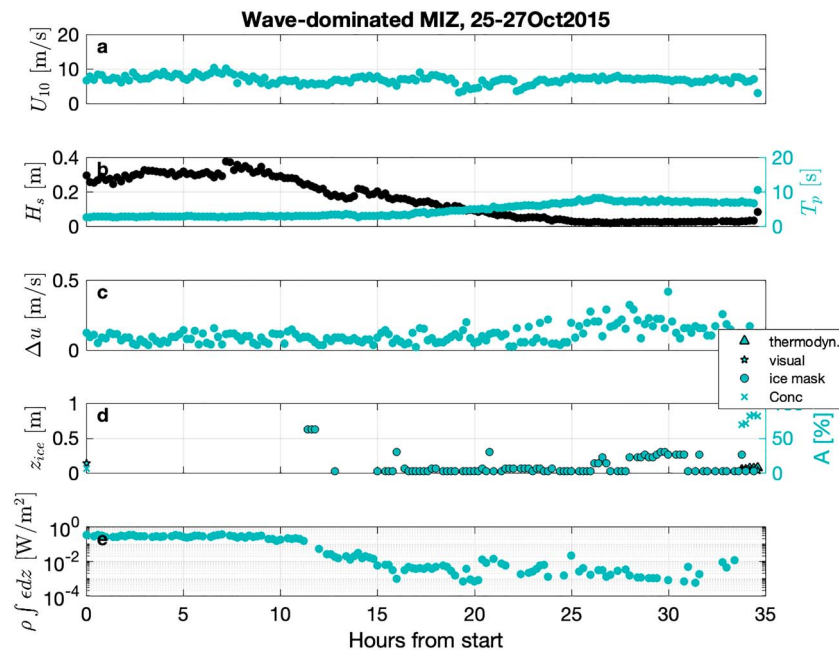


Figure 5. Time series from SWIFT deployed in wave-transferred marginal ice zone (MIZ), 25–27 October 2015 of (a) 10-m wind speed, (b) significant wave height and peak wave period, (c) relative velocity of ice and ocean (at 1.5-m depth), (d) ice thickness and concentration estimates, and (e) vertically integrated turbulent kinetic energy dissipation rates.

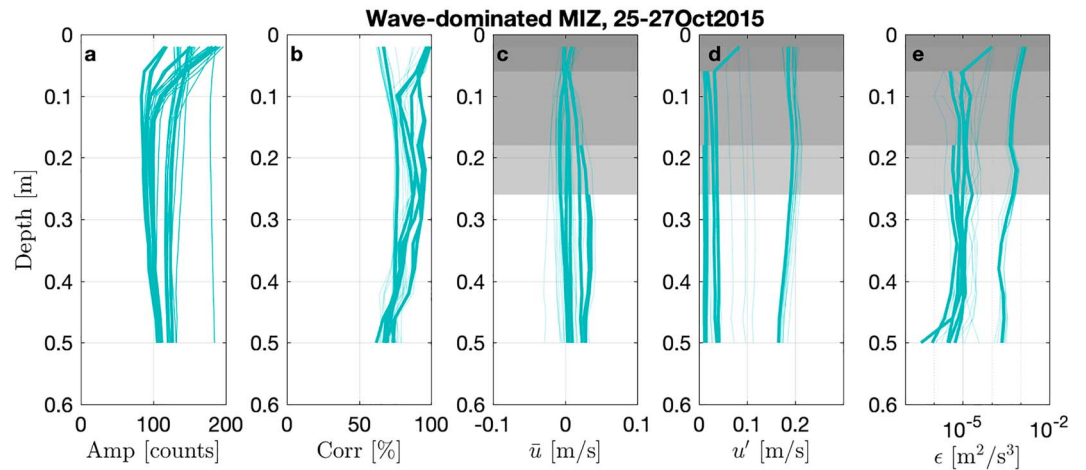


Figure 6. Aquadopp burst data from SWIFT deployed in wave-transferred marginal ice zone (MIZ), 25–27 October 2015. Vertical profiles of (a) amplitude, (b) pulse correlation, (c) average velocity, (d) turbulent velocity, and (e) dissipation rate. Thick lines indicate averages binned by ice mask, and gray shading corresponds to ice mask for each bin.

throughout the whole observation period due to the presence of significant ice. The bin-averaged dissipation rate profiles show that dissipation still decays with depth.

The examples of each of the three turbulent transfer regimes demonstrate the processes controlling the balance of wind work and turbulent dissipation. In open water (Figures 3 and 4), the integrated TKE dissipation rate decreases with declining wind speed. In the wave-transferred MIZ example (Figures 5 and 6), dissipation rates decrease with declining wave height and increasing ice, rather than any change in the wind (which is relatively constant in time). In the ice-transferred MIZ example (Figures 7 and 8), dissipation is more variable over time but appears to be most closely tied to changes in the wind and relative ice-ocean velocity (Δu). The physical mechanisms distinguishing the wave-transferred and ice-transferred MIZ regimes are explored further in the next sections using the full data set and spanning a range of conditions. Table 1 sum-

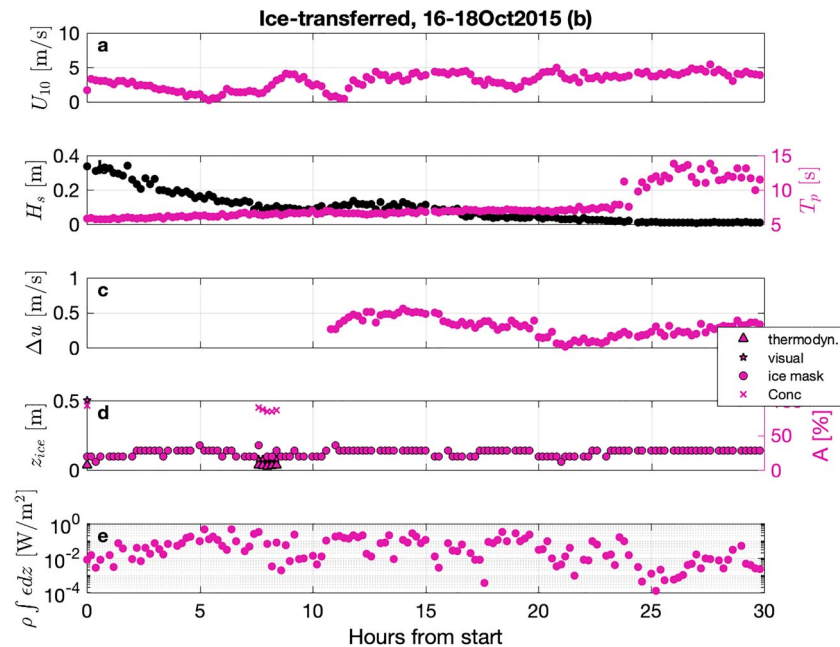


Figure 7. Time series from SWIFT deployed in ice-transferred marginal ice zone, 16–18 October 2015 (b) of (a) wind speed, (b) significant wave height and peak wave period, (c) relative velocity of ice and ocean (at 1.5-m depth), (d) ice thickness and concentration estimates, and (e) vertically integrated turbulent kinetic energy dissipation rates.

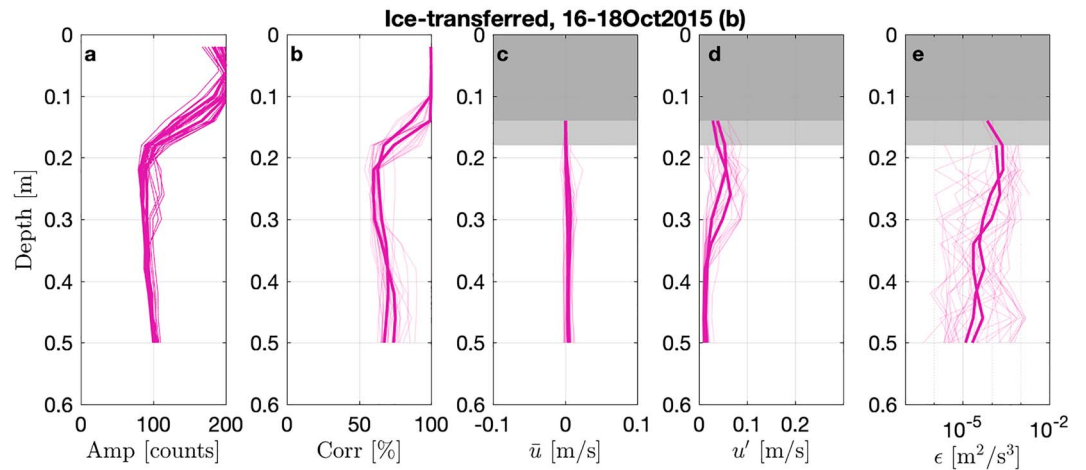


Figure 8. Aquadopp burst data from SWIFT deployed in ice-transferred marginal ice zone, 16–18 October 2015 (b). Vertical profiles of (a) amplitude, (b) pulse correlation, (c) average velocity, (d) turbulent velocity, and (e) dissipation rates. Thick lines indicate averages binned by ice mask, and gray shading corresponds to ice mask for each bin.

marizes characteristic values of key variables, but the subsequent analysis uses full time series of observed values as shown in the figures in Supporting Information S1.

As we are interested in understanding what controls enhanced turbulence at the surface above background levels, subsequent presentations of integrated dissipation rates, $\rho \int \epsilon dz$, all have an average offset removed. The offset for each deployment is calculated as the integrated value using the average of the measured dissipation rate at the bottom of the profile, $z = 0.5$ m, which is generally the lowest magnitude of ϵ in the profile.

3.2. Open Water (No Ice)

The input rate of TKE in open water is calculated as $c_e \tau_{wind}$ using measured wind stress and estimates of open water effective transfer velocity. Effective transfer speed is estimated using a typical parameterization based on wave age,

$$c_e \approx c_{eo} \left(\frac{c_p}{U_{10}} \right), \quad (6)$$

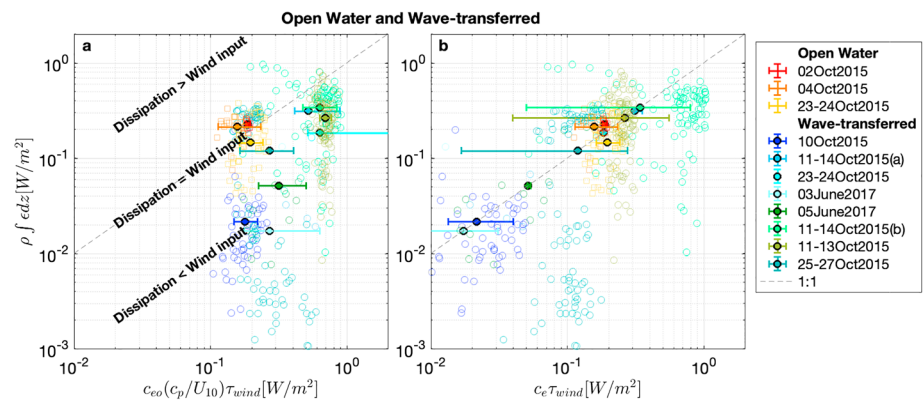


Figure 9. (a) Comparison of vertically integrated turbulent kinetic energy dissipation rates with input rate from wind expected based on open water conditions. (b) The same comparison where input rate for the wave-transferred marginal ice zone (MIZ) uses effective transfer velocities determined assuming a balance of wind input and observed dissipation rates. Each color represents a SWIFT deployment (warm colors represent open water and cool colors represent wave-transferred MIZ), and filled points represent averages for each deployment. Bars represent the range of measured drag coefficients, when applicable. Dashed black line is the 1:1 line, where expected input and dissipation are equal. Wave-transferred MIZ bin averages in (b) have been forced to lie on the line.

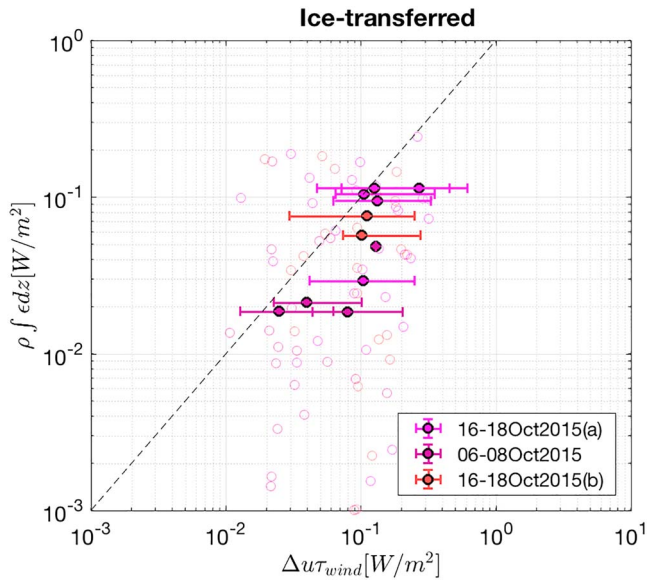


Figure 10. Comparison of vertically integrated turbulent kinetic energy dissipation rates and expected input rate from ice to ocean in marginal ice zones where wind stress is ice-transferred. Each color represents a SWIFT deployment, and filled points represent ice-mask binned averages. Error bars represent the range of measured drag coefficients. Dashed black line is 1:1 line, where expected input and observed dissipation are equal.

We find effective transfer velocities in the wave-transferred MIZ in the range of 0.01–0.8, with most clustered around 0.1–0.5. In contrast with typical relationships in open water, the MIZ transfer velocities do not depend on wave age. Instead, the MIZ effective transfer velocities have a positive correlation with wave height, and a negative correlation with ice thickness and concentration (to be shown later as a combined parameter in section 4.1).

3.4. Ice-Transferred MIZ

When the sea state is low, the roughness of the surface is set primarily by the ice, rather than the waves. The observed drag coefficients (C_d) in this regime are lower as a result of the milder wind and wave conditions and higher ice concentrations. The input of TKE from the wind to the ocean is then mediated by the motion of the ice. For these conditions, we test the concept of an effective transfer velocity that is set by the relative velocity between ice and upper ocean, Δu , such that the rate of wind work is

$$c_e \tau_{\text{wind}} = \Delta u \tau_{\text{wind}}. \quad (7)$$

Similar to the relationship of the open water transfer velocity to the wave speed, the proposed transfer velocity $c_e = \Delta u$ is intended as a characteristic velocity scale, rather than a quantitative description of the shear velocity. This assumes that the ice is moving at a constant speed relative to the ocean, such that work is being transferred through the ice (and not being done on the ice).

This parameterization of TKE energy input rate from the wind is moderately correlated with the observed integrated dissipation rate under ice, as shown in Figure 10. Hourly measurements are represented by open circles, and bin averages by ice mask depth are shown as filled circles. Bars represent the standard error of the averages, but not the error associated with velocity or wind stress measurements, both of which may be significant. Bin averages are necessary to satisfy the assumption that the material derivative of turbulence is zero, and averaging over similar ice conditions is most appropriate, as changing ice thickness is expected to most significantly change the total TKE. A linear fit to the bin-averaged measurements has a coefficient of determination $R^2 = 0.50$ and probability of false correlation $P = 0.015$. We note that when all hourly measurements are used for a linear fit, the significance decreases substantially with an $R^2 = 0.02$ and $P = 0.20$. The binned averages are all within an order of magnitude of the 1:1 line, and the overall dependence is consistent with increasing TKE dissipation rates in the presence of increasing wind input rates.

where c_p is the wave phase speed at the peak of the spectrum, and U_{10} is the wind speed (Terray et al., 1996; Thomson et al., 2016). The canonical effective transfer speed typical in open water is $c_{eo} = 2$ m/s, and the wave age dependence is weak (Thomson et al., 2016). The open water points (warm colors) in Figure 9 show that this wind input rate balances with the observed vertically integrated dissipation rates, consistent with previous studies in open water. Each open point represents an hourly value, and filled points represent averages from each deployment. The dynamic range observed is small, but the open water balance is not the focus of the present study.

3.3. Wave-Transferred MIZ

Measurements in the MIZ with waves present are plotted on Figure 9a (cool colors) using the open water parameterization for effective transfer velocity in equation (6). Dissipation rates are lower than the expected input rate (i.e., points are below the 1:1 line). Deployments from 11–14 October had larger wind stress observations than the deployments in open water, and yet the observed integrated dissipation rates are comparable. Zippel and Thomson (2016) argue that dissipation rates in the MIZ are reduced as a result of lower effective transfer velocities in ice cover. We can estimate appropriate effective transfer velocities (c_e) for these deployments by assuming that observed dissipation rates in the wave-transferred MIZ are in equilibrium with local energy input from wind, as in equation (2). Figure 9b shows the same comparison of wind input and observed integrated dissipation, where c_e values for the MIZ cases have been determined using the assumption of equilibrium.

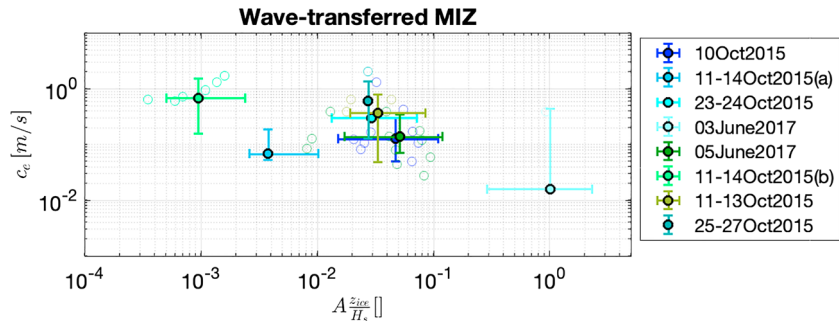


Figure 11. Effective transfer velocity in wave-transferred marginal ice zone (MIZ) using the results of Figure 9, as a function of nondimensional ratio of wave height, ice concentration, and ice thickness ($A \frac{z_{ice}}{H_s}$). Each color represents a deployment in the wave-transferred MIZ.

4. Discussion

4.1. Scaling Turbulent Regimes in the MIZ

When waves are the dominant roughness in the MIZ, the effective transfer velocity is expected to be a function of wave and ice characteristics. Zippel and Thomson (2016) examined controls on the transfer velocity and input rate in brash ice (small fragments of ice, <2 m, formed from the wreckage of other types) and found that the effective transfer velocity in brash ice decreased with increasing ice concentration. The measurements used in this study were all made in frazil ice cover (a collection of loose ice crystals) and pancake ice cover (round pieces of ice formed by waves), both of which form in turbulent conditions.

The transfer velocity is primarily associated with the high frequency waves that dominate surface roughness. High frequency waves in the equilibrium range have been shown to be a strong function of ice cover, and the magnitude of spectral damping varies with the ice characteristics (Rogers et al., 2016). It is then essential to consider ice characteristics in addition to the wave height, as the magnitude of damping at high frequencies may not be fully reflected in the significant wave height (which is weighted toward the swell waves). The effective transfer velocity is expected to decrease with increasing ice volume, by increasing concentration or thickness, and decreasing wave heights.

In Figure 11, we compare a proposed scaling parameter incorporating wave and ice conditions, $A \frac{z_{ice}}{H_s}$, with the effective transfer velocity in ice, determined by assuming local wind input and dissipation are precisely balanced (Figure 9b). Note that here A is the fractional areal coverage of ice, with a maximum value of 1, rather than the percent concentration. This nondimensional parameter and the effective transfer velocity appear to be related by a power law with the form:

$$c_e = a \left(A \frac{z_{ice}}{H_s} \right)^b. \quad (8)$$

This parameterization is for the regime where transfer in the MIZ is dominated by surface waves, so it will not be valid at the limit as H_s approaches zero where transfer is dominated by ice. The upper limit on this parameterization will be the open ocean transfer velocity (equation 6) at very small values of $A z_{ice}$.

Applying a power law fit yields values for the coefficients $a = 0.11 \pm 0.10$ m/s and $b = -0.23 \pm 0.20$, with a coefficient of determination $R^2 = 0.45$ and a probability of false correlation $P = 0.25$. Although these coefficients are not well constrained by the small number of measurements in this study, the formulation may be useful for future studies. Thickness is likely necessary to parameterize changes in the TKE input rate for these new-ice conditions, as thickness represents a larger change in total ice volume in the relatively thin pancake and frazil ice. In the thicker brash ice of Zippel and Thomson (2016), the percent change in volume is mostly described by changes in concentration.

Combining parameterizations for the effective transfer velocity in the wave-transferred and ice-transferred MIZs allows estimation of near-surface turbulent dissipation from open water into thin, new ice cover using the effective transfer framework of equation (2). The effective transfer velocity c_e is found to be a function of the wave and ice conditions which control roughness. When conditions are such that turbulence production is likely to be transferred via waves, the transfer velocity can be estimated using estimates of ice thickness, concentration, and significant wave height. When conditions are such that turbulence production is likely

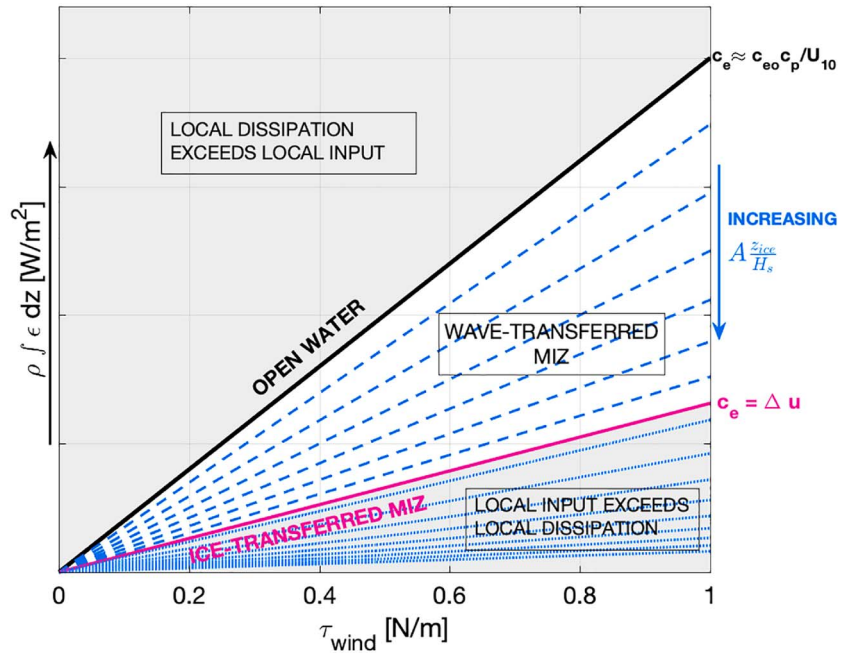


Figure 12. Schematic representation of integrated near-surface dissipation rate predicted as a function of wind stress, on the x axis, and the effective transfer velocity, given by the slope of each line. This result assumes a local balance of turbulence production from wind input and dissipation. The largest dissipation rate will occur in open water conditions, where transfer velocity c_e in a young wave field is typically twice the wave age (black line; Thomson et al., 2016). The effective transfer velocity in ice decreases as the ice increases and the wave height decreases, such that the ratio A^z_{ice}/H_s increases (blue lines). Typically, the smallest dissipation rates will be observed when the effective transfer velocity is set by the relative ice-ocean velocity, Δu (purple line), as is commonly seen in nearly 100% ice cover. Gray shaded areas represent regimes where local production and dissipation are not in balance.

to be transferred via ice, the effective transfer velocity is the change in near surface velocity (Δu). Then, the dependencies of the effective transfer velocity through these three regimes can be summarized by the piecewise function:

$$c_e \approx \begin{cases} c_{eo} \left(\frac{c_p}{U_{10}} \right) & \text{OPEN WATER} \\ a \left(A^z_{ice} / H_s \right)^b & \text{WAVE-TRANSFERRED MIZ} \\ \Delta u & \text{ICE-TRANSFERRED MIZ.} \end{cases} \quad (9)$$

The resulting estimates of integrated near-surface dissipation are shown schematically in Figure 12. Our representation of this piecewise function suggests that the transfer velocity in the wave-transferred MIZ is bound by the transfer velocities in open water and the ice-transferred MIZ, that is, $c_{eo} \left(\frac{c_p}{U_{10}} \right) > a \left(A^z_{ice} / H_s \right)^b > \Delta u$. It is hypothetically possible for Δu values to approach open water transfer velocity values, although velocities are typically an order of magnitude lower in this data set.

It is clear in Figure 12 that the local dissipation in the MIZ regimes described will always be lower than in open water. The parameterization for the ice-transferred MIZ is additionally expected to represent an upper bound on the work done by the wind on the ocean, as the parameterization for the effective transfer velocity relies on the assumption that the relative velocity between ice and ocean is constant (i.e., ice is not accelerating). The observed integrated TKE dissipation rates in Figure 10 are lower than those predicted by the parameterization, possibly indicating some additional work is being done on the ice.

These predictions provide estimates for the vertically integrated dissipation in the near surface (upper 0.5 m). In all cases, the dissipation rate maximum is at the surface (or the base of the ice) and

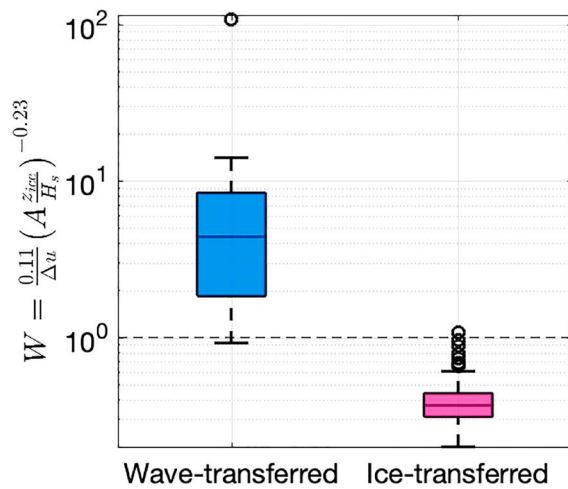


Figure 13. Boxplot of scaling parameter, W (equation (10)), calculated for SWIFT deployments in wave-transferred marginal ice zone (blue) and ice-transferred marginal ice zone (purple). Boxes contain interquartile range of data, and whiskers contain data within 2.7σ of median. Dashed line at $W = 1$ indicated proposed threshold for transition in dominant generation mechanism.

monotonically decreasing with depth. Although the total dissipation clearly depends on the extent of the vertical integral, the steep vertical profiles suggest that the majority of the dissipation occurs within 0.5 m of the surface.

These results suggest that turbulence production can be parameterized in either MIZ regime based on wave and ice conditions; however, it is necessary to determine whether wind work is wave-transferred or ice-transferred. We introduce a nondimensional scaling parameter, which we call W , representing the ratio of wave-transferred and ice-transferred transfer velocities. This parameter can be used to determine whether wind input to waves or input ice dominates near-surface turbulence and can be related to observed ice and wave conditions based on the power law fit (Figure 11) in equation (8), such that

$$W = \frac{0.11}{\Delta u} \left(A \frac{z_{\text{ice}}}{H_s} \right)^{-0.23} \quad (10)$$

We expect that when this parameter is high, input from wind will be wave-transferred, and when it is low, input will be ice-transferred.

The range of values of W calculated for SWIFT deployments categorized as wave-transferred and ice-transferred is summarized in Figure 13. This figure includes all measurements in each regime where all four of the

required variables are available ($n = 65$ in the wave-transferred MIZ regime; $n = 107$ in the ice-transferred MIZ regime). We expect conditions associated with this value to be quasi-steady, such that they vary on the hourly time scale. The Δu time series, which has measurements every 12 min, has substantial temporal noise associated with the challenge of using a narrow-band Doppler measurement in the low scattering environment of the Arctic. This velocity time series was smoothed using the moving average method with a span of 3, such that the resulting time series represents changes over 36-min periods.

Values of W are expected to be lower for observations in the ice-transferred MIZ than for observations in the wave-transferred MIZ, as the observations were initially sorted qualitatively based on small waves and high ice concentration (as described in section 2.1). Additionally, we find that wind stress in the MIZ is generally wave-transferred if $W > 1$ and ice-transferred if $W < 1$. This parameter provides a more quantitative and less subjective method for separating observations in future work. As this nondimensional parameter is derived from the ratio of transfer velocities, this result indicates that the wind stress will drive turbulence generation through the roughness element with the fastest characteristic velocity. The turbulence generation can then be parameterized the same way in both MIZ regimes, using the largest relevant transfer velocity.

The application of the scaling and equations for approximate dissipation should be limited to a similar range of conditions as those observed, with low to moderate sea state and thin, new sea ice cover. These conditions are most common during the autumn and winter near the advancing ice edge. Additionally, following the assumption of a local energy balance, it is necessary to average over the time scale in which ice conditions are relatively constant to ensure stationarity.

Products of ice thickness, wind speed, and wave height are available for many areas by satellite and/or reanalysis products and may be useful for large-scale estimates of turbulence from this method. Wind and wave data may be obtained from the ERA-Interim reanalysis (Dee et al., 2011), for example, but it should be noted there has been little validation of the wave results in sea ice cover. Comparison of different available sea ice thickness products can be found in Labe (2017). In particular, skill in measuring thin sea should be considered, which has been suggested to be well captured by microwave techniques. The relative ice-ocean velocity cannot be estimated from remote sensing products, and caution should be used in replacing with other velocity estimates such as ice drift speed, which was found to have low correlation in these data (not shown). The relative ice-ocean velocity is likely best estimated currently with coupled models (Yang, 2006).

It is possible to parameterize the observed changes in TKE dissipation rates in other ways, such as a model in which the effects of ice on near-surface turbulence is fully accounted for by reduction of wind stress into the ocean (i.e., by application of equation (1)). Although this model may be more in line with what has been

previously applied for partially ice-covered oceans (e.g., Yang, 2006), the thin MIZ may be more dynamically similar to open ocean, and thus, application of the open water effective transfer velocity framework may be more appropriate. Additionally, such a model would require detailed observations of ice-ocean stress, which we do not have here. Observations of wind stress, as we have in this study, are more commonly available and often made from ships.

4.2. Buoyancy Flux

It has been previously suggested that near-surface buoyancy production during sea ice formation may provide an additional source of turbulence. Lacking a direct estimate of the buoyancy flux, we make a rough estimate for the observations with the greatest ice growth (25–27 October) using the approximate freshwater flux. The total increase in ice volume over the approximately 6-hr deployment corresponds to a negative freshwater flux of $1.1 \text{ m}^3/\text{day}$. This corresponds to an approximate salt flux of 3.5×10^{-5} , which is converted to a buoyancy flux of $3.5 \times 10^{-6} \text{ m}^2/\text{s}^3$ by multiplying by g/ρ . Referring back to the dissipation rates in Figure 6, we see that this estimate of buoyancy flux is small compared to the observed dissipation values, even during this case of rapid ice growth. Buoyancy is only likely to become a significant source when wind input via waves and ice is sufficiently low, and ice formation is exceptionally rapid.

4.3. Dissipative Mechanisms for Waves in Ice

Turbulence under ice has been proposed as a possible key dissipative mechanism for wave energy in MIZs (Kohout et al., 2011). Although the attenuation of wave energy in the MIZ has been extensively studied and significant work is ongoing to parametrize attenuation rates (i.e., Cheng et al., 2017), the actual mechanisms are still an open question. By using winds as the universal source of upper ocean turbulence, communicated by either waves or sea ice, the present study has excluded the possibility that observed turbulence is caused directly by attenuation of waves propagating through the ice.

Although our approach is inherently focused on under-ice turbulence due to local wind input, our observations of turbulent dissipation rates do not point to near-surface turbulence as a strong attenuation mechanism. We observe that turbulence is always suppressed in the MIZ compared to open water values (Figure 9). In open water, similar wind stresses as those we observed in the MIZ would result in significantly larger dissipation values to maintain the expected balance. However, the wind input to waves in the MIZ is not well-constrained; the 1:1 line from the open water parameterization (Figure 9) thus is an upper bound on what the dissipation in the MIZ would need to exceed for wave attenuation to occur. The strong correlation of winds and waves in the young, often fetch-limited, seas of these data sets prevents a rigorous isolation of these mechanisms.

The relative importance of wave attenuation via turbulence is likely different across the various conditions observed here. Closer examination of time series of observations from one deployment in the wave-transferred MIZ shows that the rapid drop of turbulent dissipation with increasing ice (Figure 5) occurs well before the decrease in wave energy, such that turbulent dissipation is unlikely to account for the observed wave attenuation over time. This case is particularly illustrative, as the winds are mostly constant over time, such that the changes in waves are coupled to changes in ice, rather than wind. If this relationship holds in ice-transferred conditions, as well, then the decrease in energy input from wind to waves will correspond to a decrease in energy lost from the wave field to the upper ocean as turbulence. As in the wave-transferred MIZ, we find that the values of near-surface turbulent dissipation when ice controls the wind input are almost always lower than those observed in open water (Figure 10).

Although some energy will be lost from the wave field to turbulent dissipation via wave breaking and/or ice-ocean shear in both MIZ regimes, these results suggest that local wind input is a key driver of turbulent dissipation. The observed turbulent dissipation rates can largely be accounted for by the local wind. It is thus challenging to decouple local input via wind and input from attenuation of wind seas over the MIZ. Additionally, comparison of wave attenuation coefficients (calculated by Cheng et al., 2017) with integrated dissipation shows that attenuation rates are not correlated with observed local dissipation rates. Direct contributions to turbulence from wave energy may be significant under some MIZ conditions outside of those observed here and are likely to be significant under larger, thicker ice floes. Further work is necessary to determine which of the other possible mechanisms for dissipation of wave energy are important, and under what conditions they apply. For the new, thin ice herein, other dissipative mechanisms such as viscous drag within the ice layer or floe-floe collisions (Shen & Squire, 1998) may be key mechanisms for wave attenuation.

5. Conclusions

This study uses observations to build a framework for estimating near-surface turbulent dissipation rates in MIZs with relatively thin ice. Here “thin ice” is used to describe newly formed frazil and pancake ice, where the ice thickness is approximately 50 cm or less. The near-surface turbulent dissipation rate is a function of the total wind stress, which does work on the ocean at an effective transfer rate. This is the characteristic speed at which roughness elements move in the dynamic boundary layer and will be either be related to the wave or ice speed in new MIZs. In situ measurements of turbulence dissipation profiles across a range of conditions in newly formed sea ice allow parameterization of the effective transfer velocities controlling TKE input rate. We have introduced a scaling parameter, W , which may be used to determine the dominant roughness elements controlling the rate of wind work on the ocean, based on observed or estimated sea ice thickness and concentration, wave height, and relative ice-ocean shear velocity. Energy input rate for turbulence generated by wind may then be estimated using calibrated relationships determined by this study.

We do not observe under-ice dissipation values that exceed wind input rates in the MIZ, and as such, we speculate that wave attenuation modulates turbulent dissipation but does not cause it directly. In other words, local wind input may be more important than dissipation of wave energy from remote sources (i.e., attenuation of swell waves) for the generation of turbulence in thin, young MIZs.

These results build on those of Zippel and Thomson (2016) and others to provide parameterizations for near-surface turbulent dissipation in the MIZ. These may be applied for the purposes of estimating gas exchange, heat, and momentum transport. Further field and lab measurements of turbulent dissipation are necessary to improve physical understanding of mechanisms and expand parameterizations to a wider variety of conditions. In particular, different parameterizations will likely be necessary for older and thicker sea ice, including brash ice, based on measurements in those conditions.

Acknowledgments

Thanks to APL-UW Field Engineers A. de Klerk and J. Talbert for building and assisting with deployment of SWIFT buoys. Thanks also to the crews of the R/V *Sikuliaq* and R/V *Palmer* for supporting data collection. Thank you to S. Zippel and S. Stammerjohn for helpful discussion and comments and to O. Persson for providing drag coefficients. Funding was provided by the Office of Naval Research as part of the “Sea State and Boundary Layer Physics of the Emerging Arctic Ocean” Departmental Research Initiative under funding awards N00014-13-1-0284 and N00014-17-1-2544. The PIPERS program was supported by the National Science Foundation. Sea State data are available at www.apl.uw.edu/arcticseastate under the Data tab.

References

- Agrawal, Y., Terray, E., Donelan, M., Hwang, P., Williams, A. III, Drennan, W., et al. (1992). Enhanced dissipation of kinetic energy beneath surface waves. *Nature*, *359*(6392), 219.
- Ardhuin, F., Sutherland, P., Doble, M., & Wadhams, P. (2016). Ocean waves across the Arctic: Attenuation due to dissipation dominates over scattering for periods longer than 19 s. *Geophysical Research Letters*, *43*, 5775–5783. <https://doi.org/10.1002/2016GL068204>
- Bigdeli, A., Hara, T., Loose, B., & Nguyen, A. (2018). Wave attenuation and gas exchange velocity in marginal sea ice zone. *Journal of Geophysical Research: Oceans*, *123*, 2293–2304. <https://doi.org/10.1002/2017JC013380>
- Cheng, S., Rogers, W. E., Thomson, J., Smith, M., Doble, M. J., Wadhams, P., et al. (2017). Calibrating a viscoelastic sea ice model for wave propagation in the Arctic fall marginal ice zone. *Journal of Geophysical Research: Oceans*, *122*, 8770–8793. <https://doi.org/10.1002/2017JC013275>
- Dee, D. P., Uppala, S., Simmons, A., Berrisford, P., Poli, P., Kobayashi, S., et al. (2011). The ERA-Interim reanalysis: Configuration and performance of the data assimilation system. *Quarterly Journal of the Royal Meteorological Society*, *137*(656), 553–597.
- Doble, M. J., & Bidlot, J.-R. (2013). Wave buoy measurements at the Antarctic sea ice edge compared with an enhanced ECMWF WAM: Progress towards global waves-in-ice modelling. *Ocean Modelling*, *70*, 166–173.
- Gallaher, S. G., Stanton, T. P., Shaw, W. J., Cole, S. T., Toole, J. M., Wilkinson, J. P., et al. (2016). Evolution of a Canada Basin ice-ocean boundary layer and mixed layer across a developing thermodynamically forced marginal ice zone. *Journal of Geophysical Research: Oceans*, *121*, 6223–6250. <https://doi.org/10.1002/2016JC011778>
- Gemmrich, J., Mudge, T., & Polonichko, V. (1994). On the energy input from wind to surface waves. *Journal of Physical Oceanography*, *24*(11), 2413–2417.
- Grare, L., Lenain, L., & Melville, W. K. (2018). Vertical profiles of the wave-induced airflow above ocean surface waves. *Journal of Physical Oceanography*, *48*, 2901–2922.
- Guest, P. S., & Davidson, K. L. (1991). The aerodynamic roughness of different types of sea ice. *Journal of Geophysical Research*, *96*(C3), 4709–4721.
- Kohout, A. L., & Meylan, M. H. (2008). An elastic plate model for wave attenuation and ice floe breaking in the marginal ice zone. *Journal of Geophysical Research*, *113*, C09016. <https://doi.org/10.1029/2007JC004434>
- Kohout, A. L., Meylan, M. H., & Plew, D. R. (2011). Wave attenuation in a marginal ice zone due to the bottom roughness of ice floes. *Annals of Glaciology*, *52*(57), 118–122.
- Labe, Z. (2017). The climate data guide, sea ice thickness data sets: Overview and comparison table. National Center for Atmospheric Research Staff.
- Lohrmann, A., Pedersen, T., Nylund, S., & Siegel, E. (2011). Waves in the summer ice in the winter. In *Proceedings of the Current, waves and turbulence measurements (CWTM), 2011 IEEE/OES 10th* (pp. 150–158): IEEE.
- Loose, B., McGillis, W. R., Perovich, D., Zappa, C. J., & Schlosser, P. (2014). A parameter model of gas exchange for the seasonal sea ice zone. *Ocean Science*, *10*(1), 17–28.
- Lund, B., Graber, H. C., Smith, M., Doble, M., Persson, O., Thomson, J., & Wadhams, P. (2018). Arctic sea ice drift measured by shipboard marine radar. *Journal of Geophysical Research: Oceans*, *123*, 4298–4321. <https://doi.org/10.1029/2018JC013769>
- Magnell, B., Ivanov, L., & Siegel, E. (2010). Measurements of ice parameters in the Beaufort sea using the Nortek AWAC acoustic Doppler current profiler. In *Proceedings of the Oceans 2010 conference, MTS/IEEE, Seattle, WA*.
- Morison, J., McPhee, M., Curtin, T., & Paulson, C. (1992). The oceanography of winter leads. *Journal of Geophysical Research*, *97*(C7), 11199–11218.

- Persson, P. O. G., Blomquist, B., Guest, P., Stammerjohn, S., Fairall, C., Rainville, L., et al. (2018). Shipboard observations of the meteorology and near-surface environment during autumn freeze-up in the Beaufort/Chukchi Seas. *Journal of Geophysical Research: Oceans*, *123*, 4930–4969. <https://doi.org/10.1029/2018JC013786>
- Persson, P. O. G., Fairall, C. W., Andreas, E. L., Guest, P. S., & Perovich, D. K. (2002). Measurements near the atmospheric surface flux group tower at Sheba: Near-surface conditions and surface energy budget. *Journal of Geophysical Research*, *107*(C10), 8045. <https://doi.org/10.1029/2000JC000705>
- Rogers, W. E., Thomson, J., Shen, H. H., Doble, M. J., Wadhams, P., & Cheng, S. (2016). Dissipation of wind waves by pancake and frazil ice in the autumn Beaufort Sea. *Journal of Geophysical Research: Oceans*, *121*, 7991–8007. <https://doi.org/10.1002/2016JC012251>
- Shen, H. H., & Squire, V. A. (1998). Wave damping in compact pancake ice fields due to interactions between pancakes. *Antarctic Sea Ice: Physical Processes, Interactions, and Variability*, *74*, 325–341.
- Smith, M., Stammerjohn, S., Persson, O., Rainville, L., Liu, G., Perrie, W., et al. (2018). Episodic reversal of autumn ice advance caused by release of ocean heat in the Beaufort Sea. *Journal of Geophysical Research: Oceans*, *123*, 3164–3185. <https://doi.org/10.1002/2018JC013764>
- Spren, G., Kaleschke, L., & Heygster, G. (2008). Sea ice remote sensing using AMSR-E 89 GHz channels. *Journal of Geophysical Research*, *113*, C02S03. <https://doi.org/10.1029/2005JC003384>
- Steele, M., Morison, J. H., & Untersteiner, N. (1989). The partition of air-ice-ocean momentum exchange as a function of ice concentration, floe size, and draft. *Journal of Geophysical Research*, *94*(C9), 12,739–12,750. <https://doi.org/10.1029/JC094iC09p12739>
- Terray, E., Donelan, M., Agrawal, Y., Drennan, W., Kahma, K., Williams, A., et al. (1996). Estimates of kinetic energy dissipation under breaking waves. *Journal of Physical Oceanography*, *26*(5), 792–807.
- Thomson, J. (2012). Wave breaking dissipation observed with “SWIFT” drifters. *Journal of Atmospheric and Oceanic Technology*, *29*, 1866–1882. <https://doi.org/10.1175/JTECH-D-12-00018.1>
- Thomson, J., Ackley, S., Girard-Arduin, F., Arduin, F., Babanin, A., Bidlot, J., et al. (2018). Overview of the Arctic Sea state and boundary layer physics program. *Journal of Geophysical Research: Oceans*, *123*, 8674–8687. <https://doi.org/10.1002/2018JC013766>
- Thomson, J., Schwendeman, M., & Zippel, S. (2016). Wave-breaking turbulence in the ocean surface layer. *Journal of Physical Oceanography*, *46*, 1857–1870. <https://doi.org/10.1175/JPO-D-15-0130.1>
- Wadhams, P., Aulicino, G., Parmiggiani, F., Persson, P., & Holt, B. (2018). Pancake ice thickness mapping in the Beaufort Sea from wave dispersion observed in SAR imagery. *Journal of Geophysical Research: Oceans*, *123*, 2213–2237. <https://doi.org/10.1002/2017JC013003>
- Wang, X., Key, J. R., & Liu, Y. (2010). A thermodynamic model for estimating sea and lake ice thickness with optical satellite data. *Journal of Geophysical Research*, *115*, C12035. <https://doi.org/10.1029/2009JC005857>
- Wiles, P. J., Rippeth, T. P., Simpson, J. H., & Hendricks, P. J. (2006). A novel technique for measuring the rate of turbulent dissipation in the marine environment. *Geophysical Research Letters*, *33*, L21608. <https://doi.org/10.1029/2006GL027050>
- Worby, A. P. (1999). *Observing Antarctic sea ice: A practical guide for conducting sea ice observations from vessels operating in the Antarctic pack ice, a CD-ROM, Scientific Committee on Antarctic Research (SCAR) Antarctic Sea Ice Processes and Climate (ASPeCt) Program.* Hobart, Tasmania, Australia.
- Worby, A. P., Geiger, C. A., Paget, M. J., Van Woert, M. L., Ackley, S. F., & DeLiberty, T. L. (2008). Thickness distribution of Antarctic sea ice. *Journal of Geophysical Research*, *113*, C05S92. <https://doi.org/10.1029/2007JC004254>
- Yang, J. (2006). The seasonal variability of the Arctic Ocean ekman transport and its role in the mixed layer heat and salt fluxes. *Journal of Climate*, *19*(20), 5366–5387. <https://doi.org/10.1175/JCLI3892.1>
- Yu, Y., & Rothrock, D. (1996). Thin ice thickness from satellite thermal imagery. *Journal of Geophysical Research*, *101*(C11), 25,753–25,766. <https://doi.org/10.1029/96JC02242>
- Zippel, S. F., & Thomson, J. (2016). Air-sea interactions in the marginal ice zone. *Elementa Science of the Anthropocene*, *4*, 95. <https://doi.org/10.12952/journal.elementa.000095>
- Zippel, S. F., Thomson, J., & Farquharson, G. (2018). Turbulence from breaking surface waves at a river mouth. *Journal of Physical Oceanography*, *48*(2), 435–453. <https://doi.org/10.12952/journal.elementa.000095>